# Integrated photonic coupler based on frustrated total internal reflection

Nathan R. Huntoon,[1] Marc P. Christensen,[1,*] Duncan L. MacFarlane,[2] Gary A. Evans,[1] and C. S. Yeh[1]

[1]Department of Electrical Engineering, Southern Methodist University, P.O. Box 750338 Dallas, Texas 75275-0338, USA

[2]Eric Jonsson School of Engineering and Computer Science, University of Texas Dallas, P.O. Box 830688 EC33, Richardson, Texas 75083-0688, USA

*Corresponding author: mpc@engr.smu.edu

Received 16 May 2008; accepted 14 August 2008; posted 4 September 2008 (Doc. ID 96340); published 16 October 2008

An optical coupler for integrated photonic circuits is presented and analyzed. The coupler is based on frustrated total internal reflection (FTIR) and offers high efficiency in a compact footprint. Analytic expressions for the transmission and reflection coefficients of the coupler are obtained using a plane-wave theory and experimentally verified. Finite-difference time-domain modeling of FTIR is discussed and modeling results of the coupler are presented. A parametric discussion of the FTIR coupler provides design tools for making 3 dB couplers. © 2008 Optical Society of America

*OCIS codes:* 130.3120, 260.6970.

## 1. Introduction

Key components of large-scale photonic integrated circuits (PICs) are couplers that split optical signals in a waveguide into multiple waveguides with high efficiency and minimal backreflection. A conventional approach to this problem is the adiabatically tapered "Y" coupler [1–3] that achieves very high efficiencies with virtually no backreflection, but requires a length of several hundreds of micrometers. Resonant structures may also be included in Y-type couplers to reduce the size but not necessarily the group delay of the device [4]. Parallel waveguide-based directional couplers have also been realized in a variety of material systems [5–7] and, in these structures, gratings may be included to provide wavelength selectivity and shorter length scales [8–11]. Recently, compact "air trench" tapers have been demonstrated for low index contrast systems with efficiencies in the high 90% range that occupy areas of approximately $30\,\mu\text{m} \times 30\,\mu\text{m}$[12]. The large footprints of each of these coupler types put limitations on their utility in integrated optical circuits.

In this paper a coupler based on frustrated total internal reflection (FTIR) is presented. FTIR has been discussed in depth in the literature. Reference [13] provides a historical review of the development of FTIR as well as an elegant derivation of the plane-wave reflection and transmission coefficients. Investigation of the Goos–Hanchen phase shift led to the discovery of power flow between the mediums at a totally internally reflecting (TIR) interface [14]. The Goos–Hanchen shift is intimately coupled to the underlying operation of FTIR; power is transferred from the first interface to the second, thus frustrating the power reflected off the first interface. FTIR is currently being utilized in $Q$ modulators [15], laser cavity resonators [16], and microscopy [17].

Consider a photonic integrated circuit that includes a waveguide. There will be a well-established mode propagating in that waveguide. If a wide vertical trench of lower index intersects the waveguide at an angle, there will be a reflection off the first face of the trench. If the angle of the trench with respect to the waveguide direction of propagation exceeds the critical angle for the relative index change, then

0003-6935/08/305682-09$15.00/0

there will be total internal reflection and all of the power will be reflected. This has been used with thick trenches in photonic integrated circuits to turn tight corners [18]. At a TIR interface there is an exponentially decaying evanescent field extending perpendicularly into the trench. If the trench is narrow enough that this decaying field has nonnegligible amplitude at the far trench wall, then FTIR will occur and a portion of the power will continue to propagate beyond the trench. Provided that the trench extends into the waveguide such that it encompasses the whole optical mode and the trench walls are smooth, this coupling mechanism is lossless. The coupler is readily integrated in photonic circuits and can have a footprint on the order of the optical mode cross section with efficiencies in the high 90% range.

This paper develops analytic expressions for an FTIR coupler using a plane-wave approach to evaluate coupling between two waveguides. This model is verified through experimentation and finite-difference time-domain (FDTD) waveguide analysis. Finally, a parametric analysis of the 3 dB coupler is presented.

## 2. Plane-Wave Model of FTIR

In this section an analytic model of a propagating plane wave in a high-index material incident on an angled trench of low index is developed. While the actual mode is a summation of multiple plane waves that share a common propagation vector, if the mode propagation vector $\beta$ is close to the wave propagation vector $k$, for many waveguide geometries it can be well approximated by a singe plane wave traveling parallel to the waveguide. Assuming a single plane wave allows analysis of the trench with only a single angle of incidence.

The boundary conditions of this setup for a trench of width $w$ are presented below.

$$E^{\mathrm{I}}_{\mathrm{transverse}}(x,y,z=0^{-},t)=E^{\mathrm{II}}_{\mathrm{transverse}}(x,y,z=0^{+},t), \tag{1}$$

$$H^{\mathrm{I}}_{\mathrm{normal}}(x,y,z=0^{-},t)=H^{\mathrm{II}}_{\mathrm{normal}}(x,y,z=0^{+},t), \tag{2}$$

$$E^{\mathrm{II}}_{\mathrm{transverse}}(x,y,z=w^{-},t)=E^{\mathrm{III}}_{\mathrm{transverse}}(x,y,z=0^{+},t), \tag{3}$$

$$H^{\mathrm{II}}_{\mathrm{normal}}(x,y,z=w^{-},t)=H^{\mathrm{III}}_{\mathrm{normal}}(x,y,z=w^{+},t). \tag{4}$$

To solve the wave equation with these boundary conditions, standard forms of the solution are assumed. In region I the assumed form is a sum of propagating waves in the $+z$ and $-z$ directions. In region III a propagating wave in $+z$ is assumed. Region II is assumed to have the form of a sum of exponentially decaying evanescent waves, one decaying in $+z$ and one decaying in $-z$. To simplify the problem, two separate cases are considered. The first is when the electric field is transverse to the plane of incidence on the trench (TE), and the second is when the magnetic field is transverse to the plane of incidence on the trench (TM). The general solution to the problem is a superposition of these two cases.

### A. Transverse Electric

The first case discussed is when the electric field is transverse to the trench. For an incident plane wave transverse to the trench, field equations describing the incident wave are the well-known Eqs. (5)–(7):

$$H_x(x,y,t)=\hat{x}\cos(\theta_i)\frac{E_0}{\eta_1}\exp[-jk_0(x\sin(\theta_i)+z\cos(\theta_i))], \tag{5}$$

$$H_z(x,y,t)=-\hat{z}\sin(\theta_i)\frac{E_0}{\eta_1}\exp[-jk_0(x\sin(\theta_i)+z\cos(\theta_i))], \tag{6}$$

$$E_y(x,y,t)=\hat{y}E_0\exp[-jk_0(x\sin(\theta_i)+z\cos(\theta_i))]. \tag{7}$$

Applying these equations to the boundary conditions of Eqs. (1)–(4) results in four simultaneous equations with five unknowns:

$$E^{\mathrm{I}}_{\mathrm{inc}}(x,y)+E^{\mathrm{I}}_{\mathrm{ref}}(x,y)=E^{\mathrm{II}}_{+}(x,y)+E^{\mathrm{II}}_{-}(x,y), \tag{8}$$

$$E^{\mathrm{II}}_{+}\exp(-jk_0n_2\cos(\theta_2)w)+E^{\mathrm{II}}_{-}\exp(+jk_0n_2\cos(\theta_2)w)=E^{\mathrm{III}}_{\mathrm{tran}}\exp(-jk_0n_2\cos(\theta_2)w), \tag{9}$$

$$n_1\cos(\theta_1)(E^{\mathrm{I}}_{\mathrm{inc}}-E^{\mathrm{I}}_{\mathrm{ref}})=n_2\cos(\theta_2)(E^{\mathrm{II}}_{+}-E^{\mathrm{II}}_{-}), \tag{10}$$

$$n_2\cos(\theta_2)E^{\mathrm{I}}_{+}\exp(-jk_0n_2\cos(\theta_2)w)+E^{\mathrm{II}}_{-}\exp(jk_0n_2\cos(\theta_2)w)=n_1\cos(\theta_1)E^{\mathrm{III}}_{\mathrm{tran}}\exp(jk_0n_2\cos(\theta_2)w), \tag{11}$$

where $E^{\mathrm{I}}_{\mathrm{inc}}$ is the incident field in region I, $E^{\mathrm{I}}_{\mathrm{ref}}$ is the reflected field in region I, $E^{\mathrm{II}}_{+}$ is the evanescent field decaying in the $+z$ direction in region II, $E^{\mathrm{II}}_{-}$ is the evanescent field decaying in the $-z$ direction in

region II, $E_{\text{tran}}^{\text{III}}$ is transmitted field propagating in the $+z$ direction in region III, $n_1$ is the index of refraction of regions I and III, $n_2$ is the index of refraction of region II, $\theta_1$ is the incident angle from region I to region II, $\theta_2$ is the angle of the evanescent field in region II, thus the angle of incidence of the fields from region II to region III, and $k_0$ is the free-space wave vector of the incident wave.

Because this is an under-specified problem, a direct solution for all of the fields is not possible. However, what can be found is the ratio between two fields. The useful quantities for a device are: the ratio between the transmitted field in region III and the incident field in region I and the ratio between the reflected field in region I and the incident field in region I. Solving Eqs. (8)–(11) for these two ratios leads to Eqs. (12) and (13):

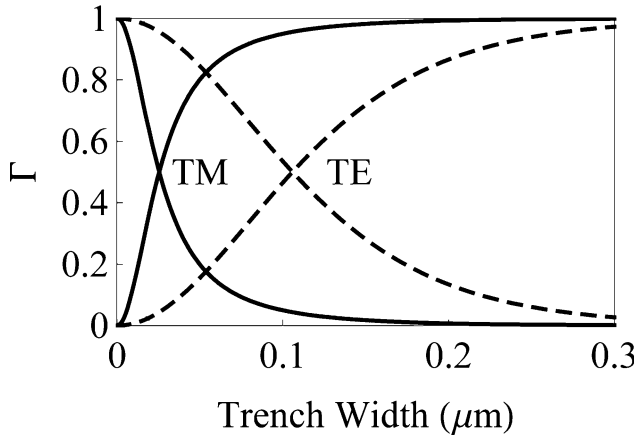


Fig. 1. Reflection and transmission coefficients for a plane wave as gap width varies from 0 to 300 nm. Waveguide index = 3.22, trench index = 1, wavelength = 1.55 $\mu$m, angle of incidence = 45°. Dashed curves, transverse electric; solid curves, transverse magnetic.

$$\frac{E_{\text{tran}}^{\text{III}}}{E_{\text{inc}}^{\text{I}}} = \frac{-4\alpha_{\text{TE}}\beta_{\text{TE}}\exp[jk_0 w(n_2\cos(\theta_2) - n_1\cos(\theta_1))]}{\alpha_{\text{TE}}^2(\exp(\delta)-1) + \beta_{\text{TE}}^2(\exp(\delta)-1) - 2\alpha_{\text{TE}}\beta_{\text{TE}}(\exp(\delta)+1)}, \tag{12}$$

$$\frac{E_{\text{ref}}^{\text{I}}}{E_{\text{inc}}^{\text{I}}} = \frac{\alpha_{\text{TE}}^2(\exp(\delta)-1) + \beta_{\text{TE}}^2(1-\exp(\delta))}{\alpha_{\text{TE}}^2(\exp(\delta)-1) + \beta_{\text{TE}}^2(\exp(\delta)-1) - 2\alpha_{\text{TE}}\beta_{\text{TE}}(\exp(\delta)+1)}, \tag{13}$$

where

$$\alpha_{\text{TE}} = n_1\cos(\theta_1), \tag{14}$$

$$\beta_{\text{TE}} = n_2\cos(\theta_2), \tag{15}$$

$$\delta = jk_0 n_2 2w \times \cos(\theta_2). \tag{16}$$

Taking the magnitude squared of Eqs. (12) and (13) yields the power transmission coefficient and power reflection coefficient, respectively.

Figure 1 shows the TE transmission and reflection coefficients for a plane wave with wavelength 1.55 $\mu$m incident at 45° upon an air trench separating two slabs of material with index of 3.22 as the trench width varies from 0 to 300 nm. Using either Eq. (12) or Eq. (13) it is possible to numerically solve for a trench width that will provide a desired reflection or transmission coefficient for a TE plane wave.

### B. Transverse Magnetic

The second case discussed is when the magnetic field is transverse to the trench. The well-known field equations for a TM wave are

$$H_y(x,y,t) = \hat{y}H_0\exp[-jk_0(x\sin(\theta_i) + z\cos(\theta_i))], \tag{17}$$

$$E_x(x,y,t) = -\hat{x}\cos(\theta_i)H_0\eta\exp[-jk_0(x\sin(\theta_i) + z\cos(\theta_i))], \tag{18}$$

$$E_x(x,y,t) = \hat{z}\sin(\theta_i)H_0\eta\exp[-jk_0(x\sin(\theta_i) + z\cos(\theta_i))]. \tag{19}$$

Applying boundary conditions (1)–(4) again and solving for the desired field ratios yields

$$\frac{E_{\text{tran}}^{\text{III}}}{E_{\text{inc}}^{\text{I}}} = \frac{4\alpha\beta(\exp(\delta/2)-1)}{\alpha_{\text{TM}}^2(\exp(\delta)-1) + \beta_{\text{TM}}^2(\exp(\delta)-1) + 2\alpha\beta(\exp(\delta)+1)}, \tag{20}$$

$$\frac{E^{I}_{ref}}{E^{I}_{inc}} = \frac{(\beta^2_{TM} - \alpha^2_{TM})(\exp(\delta/2) + 1)}{\alpha^2_{TM}(\exp(\delta) - 1) + \beta^2_{TM}(\exp(\delta) - 1) + 2\alpha_{TM}\beta_{TM}(\exp(\delta) + 1)}, \tag{21}$$

where

$$\alpha_{TM} = n_1 \cos(\theta_2), \tag{22}$$

$$\beta_{TM} = n_2 \cos(\theta_1). \tag{23}$$

and $\delta$ is again defined by Eq. (16).

Figure 1 also shows the TM transmission and reflection coefficients for the same material description given above as the trench width varies from 0–300 nm. Using either Eq. (20) or Eq. (21) it is possible to numerically solve for a trench width that will give any desired reflection or transmission coefficient for a TM wave.

### 3. Experimental Verification in the Millimeter Wave Regime

It is common practice to prototype nanoscale structures in the millimeter wave region. For example, the first photonic bandgap crystals were validated in the millimeter wave region [19] and early studies in negative refractive index materials benefited from this approach [20]. Equivalent structures and materials are fabricated at an increased wavelength by a factor of ~1000. This allows precise measurement of small (relative to the wavelength) structures. Such an approach allows novel concepts to be validated by removing the risk associated with the uncertainty involved in manufacturing errors. In this work, an experiment was done to verify the model of evanescent coupling presented above. An 88.2 GHz radio frequency (RF) source (free-space wavelength of 3.44 mm) was coupled into an alumina dielectric waveguide ($n = 3.13$) of dimensions 1 mm × 3.2 mm. The single-mode waveguide was cut at 45° and the two waveguide pieces were translated from touching to a 700 $\mu$m gap. Figure 2 shows the experimental setup of the millimeter wave experiment. The power coupled into the second waveguide was measured every 50 $\mu$m as the gap increased. The collected data was then compared to the developed theory. Figure 3 shows the good agreement between experimental data and the plane-wave model.

### 4. Finite-Difference Time-Domain Modeling of FTIR

In addition to the millimeter wave experiment presented above, the coupler was studied using the FDTD numerical modeling technique. FDTD is based on a discretization of time and space, solving Maxwell's equations using finite-difference derivatives, and employs a time marching scheme to propagate electromagnetic waves. The behavior of FDTD simulations is well understood and documented [21]. However, care must be taken when modeling evanescent fields. In particular, the selection of the spatial resolution $(\Delta x, \Delta y, \Delta z)$ has two additional considerations that must be taken into account. The first is the effect of electrically small features on evanescent fields; the second is the numerical dispersion inherent in FDTD modeling.

In general, physical features smaller than 1/10 a wavelength do not have appreciable effects on propagating electromagnetic waves. Because of this, in FDTD models, it is standard practice to make the spatial resolution slightly smaller than 1/10 of a wavelength. The coupler is dependent upon evanescent fields, though, and the concept of a wavelength is not appropriate when dealing with evanescent fields. Instead, the decay rate of the field strength is the important scale of measure. When modeling evanescent fields, the spatial resolution must be selected such that accurate sampling of the field is done before it decays to a negligible strength. Spatial resolutions of the order of 1/50 of a free-space wavelength are not unreasonable.

Inherent in the FDTD algorithm is a well-documented numerical dispersion phenomenon [22]. While there are simulation parameters that reduce the numerical dispersion of propagating waves to zero, evanescent fields have no such parameter set. The best that can be is to set the spatial and

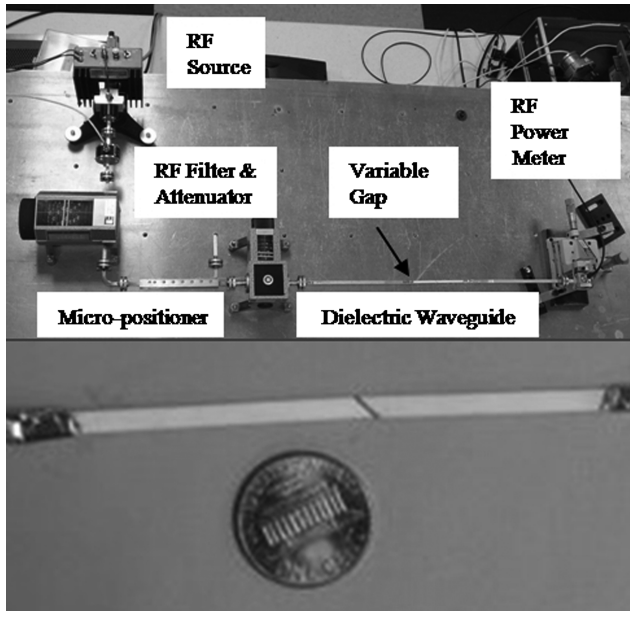


Fig. 2. Photograph of RF experimental setup verifying coupler design. 3.4 mm radiation is launched into a dielectric waveguide with a 45° cut. The gap width is varied to determine the power that evanescently couples across the gap.

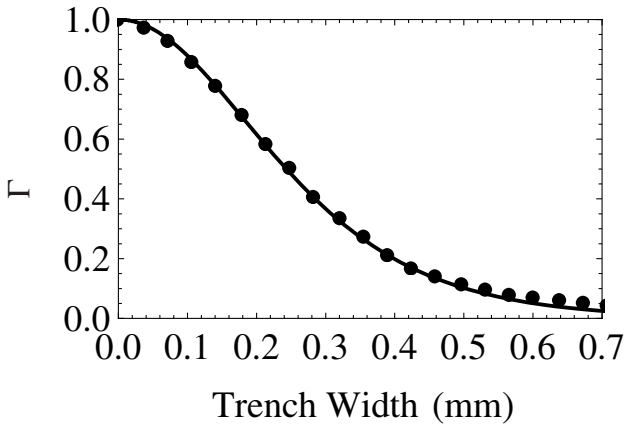


Fig. 3. Experimental and analytical results of RF evanescent coupling experiment. Dots, experimental; solid curve, analytical.

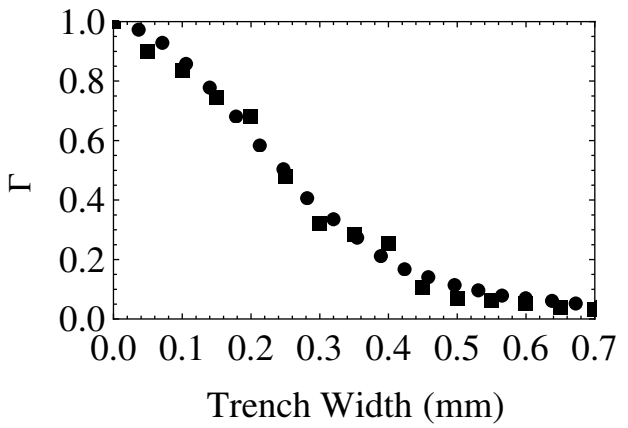


Fig. 4. Numerical and experimental results of RF evanescent coupling experiment. Dots, experimental; squares, numerical.

temporal resolution to as fine as is computational feasible to minimize the dispersion error [23].

The stability criteria for FDTD simulations relates the spatial and temporal resolutions by

$$c\Delta t = \frac{1}{(\Delta x^2 + \Delta y^2 + \Delta z^2)^{1/2}}. \tag{24}$$

Because of this, as the spatial resolution increases, so too must the temporal resolution.

These sampling constraints, particularly for the three-dimensional FDTD simulations performed in this study, set a formidable demand on the computational requirements. Specifically, the computational memory requirements increase as the cube of the spatial resolution and the computational time required for a simulation increase linearly with the temporal resolution. A multiple computer cluster dedicated to FDTD modeling was used for all of the following simulations.

### A. FDTD Simulation of Millimeter Wave Experiment

The first series of numerical calculations performed were analysis on the millimeter wave experiment described above. The physical waveguide setup described in Section 4 was modeled. The fundamental propagating mode of the waveguide was numerically solved for and launched down the waveguide. Multiple runs were done, changing the gap between the waveguide with every run. As with the experiment, the transmitted power was recorded for gap widths ranging from 0 to 700 $\mu$m. Figure 4 shows the experimental and numerical results. The close correlation verifies that FDTD is a viable technique for modeling problems involving evanescent coupling as long as appropriate modeling parameters are chosen. By having experimental data with which to compare the results, high confidence in FDTD as a modeling technique for FTIR couplers was achieved.

### B. FDTD Simulation of Optical FTIR Coupler

With FDTD verified as an accurate modeling technique for FTIR couplers, numerical calculations on a 3 dB coupler were done. Two ridge waveguides intersecting in a "T" with a narrow trench inserted at an angle of 45° across the intersection was modeled. The base material is InP with an active quantum well layer in the substrate. The ridge is 2.4 $\mu$m tall and 3.5 $\mu$m wide. This structure has a fundamental mode for light at 1.55 $\mu$m that is transverse magnetic to the plane of incidence on the trench and is approximately 7 $\mu$m in width. To have total mode overlap, the trench must be slightly longer than 7 $\mu$m. This gives the coupler a physical footprint smaller than 10$\mu$m × 10$\mu$m, nearly an order of magnitude smaller than previous couplers. The effective index of the waveguide for the fundamental mode is 3.22. Figure 5 shows a view looking down at the waveguide intersection.

To improve accuracy in modeling the trench width, the model is rotated 45°. This puts the trench parallel to a major grid axis, which provides several benefits. The simulation setup can be better controlled because precise boundaries of the trench can be determined, as well as the exact number of numerical simulation points inside the trench. Placing the trench parallel to a major axis also ensures that the evanescent fields inside the trench will be oriented along a major axis. This provides the best case for numerical dispersion.

The fundamental mode is launched from the bottom left leg, is reflected into the bottom right leg, and is transmitted to the top right leg. Power meters are placed to record the simulated reflected, transmitted, and scattered power. Three separate power meters measure scattered power; the first is in the launching waveguide measuring backscatter, the second is above the waveguide measuring radiated power, and the third is buried in the substrate below the waveguide measuring radiated power. Solving Eq. (21) numerically with an air-filled trench for a reflection coefficient of 0.5 for the above structure yields a trench width of 25 nm. Figure 6 shows the steady state $H_z$ field for a trench of 25 nm.

A series of numerical calculations were done on the model shown in Fig. 5 and presented above to investigate the reflection and transmission coefficients as

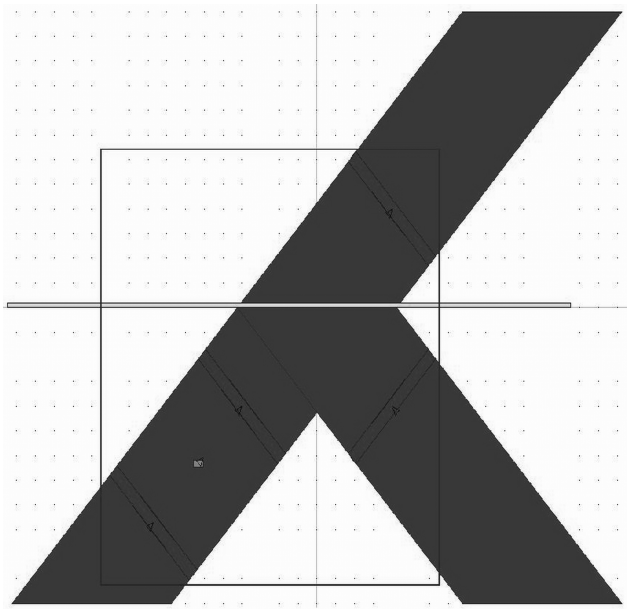

Fig. 5. FDTD model of optical FTIR coupler. The fundamental mode is launched from bottom left leg toward the "T" intersection. Reflected light travels into the bottom right leg while transmitted light travels into the top right leg. The waveguide is InP with a 3.5 $\mu$m ridge. The fundamental mode index is $n = 3.22$. The trench is at a 45° angle to the waveguide direction of propagation.

functions of the trench width. The width of the trench was scanned from 0–200 nm in steps of 20 nm. Figure 7 shows the good agreement between the analytical and numerical results at each trench width. No appreciable power was detected in any of the power meters looking for scattered power. This supports the claim that the coupler is highly efficient.

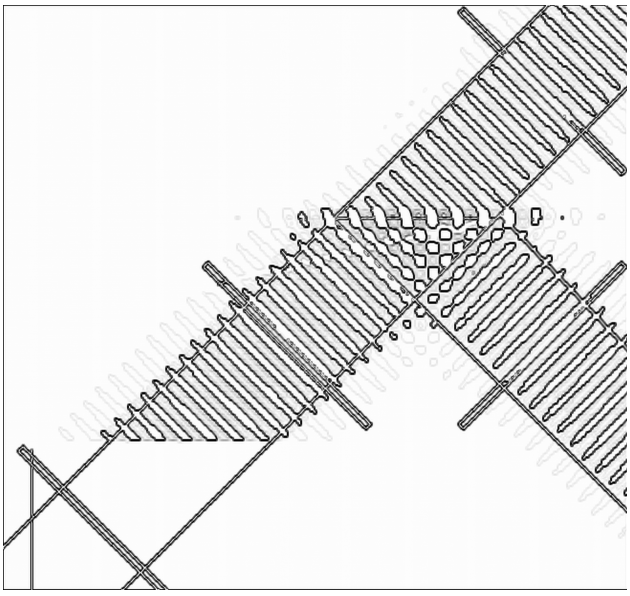

Fig. 6. Hy field distribution after FDTD run. The run proceeds long enough for steady state fields to settle. The trench is 25 nm wide filled with air, $n = 1$. Note the Goos–Hanchen shift evident in the reflected field distribution.

## 5. Design of FTIR 3 dB Coupler

There is good agreement among experiment, numerical simulation, and the analytical model presented in Section 1. Designing a device based upon the analytical model can be done with high confidence. Inspection of Eqs. (12), (13), (20), and (21) shows that, for a given wavelength, there are three variables that dictate the trench width required for a 3 dB coupler. These three variables are the waveguide index of refraction, the trench index of refraction, and the angle of incidence on the trench. A designer will often have control over at least one of these, if not more. The behavior of the optical 3 dB coupler is presented in the following as these values are varied over typical ranges. All of the presented results are based on a free-space wavelength of 1.55 $\mu$m.

The first variable to be examined is the index of refraction of the waveguide. In many optical systems this value will be set by other factors, but if the optical coupler is to be an integral part of the optical system, the behavior of the coupler needs to be considered. Figure 8 shows the trench widths required for a 3 dB coupler as the index of the waveguide varies from 1.5 to 3.5 if the trench is filled with air and the angle of incidence is 45°. This range covers most silicon-based systems up to III–V semiconductor systems. A 3 dB coupler based on FTIR can thus be integrated into many common integrated photonic circuits without having to change base materials. A notable point in Fig. 8 is the waveguide index where the TE and TM curves intersect. A coupler designed at this point would be polarization insensitive.

Because of the requirement that the trench extend deep enough into the waveguide that it totally overlaps the mode, trench depths can often be of the order of micrometers. Examination of Fig. 8 shows that the trench widths required for 3 dB is of the order of hundreds of nanometers. As the index of the waveguide approaches 2, it is less than 100 nm. This can lead to

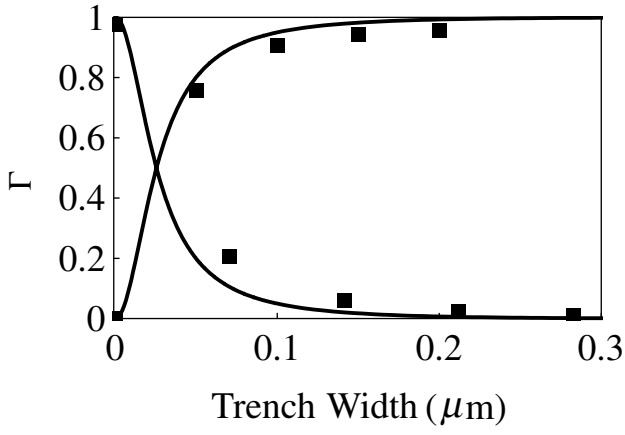


Fig. 7. Analytical and numerical results for transmission and reflection coefficients. Wavelength = 1.55 $\mu$m, angle of incidence = 45°, index of trench $n = 1$, trench width 0–200 nm. Solid curves, analytic; squares, numerical.

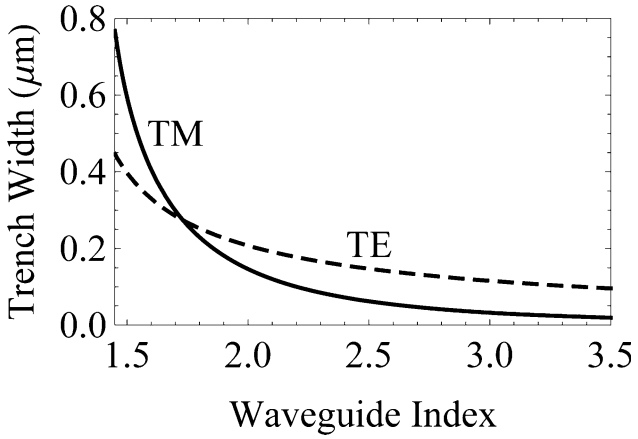


Fig. 8. Trench width required for 50% coupling as the index of refraction of the waveguide varies from $n = 1.5$ to $n = 3.5$. Dashed curve, TE; solid curve, TM.

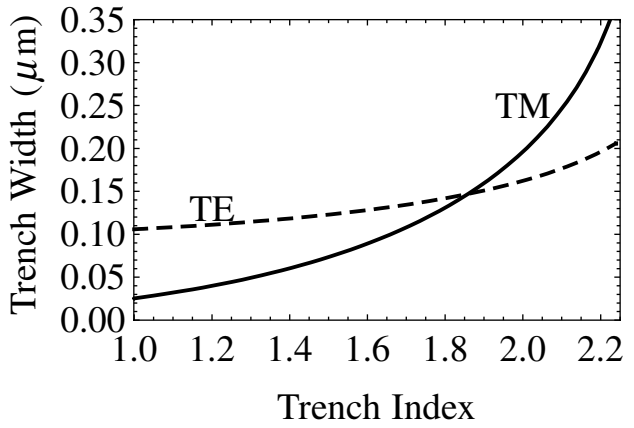


Fig. 9. Trench width required for 50% coupling as the index of refraction of the trench varies from $n = 1$ to $n = 2.5$. Dashed curve, TE; solid curve, TM.

the requirement for trenches that have a depth-to-width ratio greater than 20 to 1. Fabricating trenches with aspect ratios this high is approaching the current state of the art [24].

A method for increasing the trench width is to increase the index of refraction in the trench. Figure 9 shows the trench widths required for a 3 dB coupler as the index of the trench is varied from air, $n = 1$, to $n = 2.5$. The index of the waveguide is 3.22 and the angle of incidence is 45°. In some instances, it may be easier to fabricate a wider trench and backfill the trench with a higher-index material. Atomic layer deposition (ALD) has been successfully used to fill spaces of the order of 100 nm [25]. As with Fig. 8, a notable point in Fig. 9 is the point where the TE and TM curves intersect. This, again, is where a polarization-independent device is possible.

For the design of a 3 dB coupler with an angle of incidence of 45° and a wavelength of light of 1.55 μm, Figs. 10 and 11 summarize the above results for many common waveguide and fill materials. Figure 10 is for fields that are TE to the gap and Fig. 11 is for fields that are TM to the gap.

The final parameter to be investigated is the angle of incidence. Because FTIR depends upon an angle of incidence higher than the critical angle, this becomes the lower limit of possible angles. The upper limit on possible angles is where the trench is parallel to the waveguide. Figure 12 plots the trench widths required for 3 dB coupling as the angle of incidence is swept from the critical angle to 90°. Again, it is noted that the coupler will operate independent of polarization where the TE and TM curves intersect.

Figure 12 shows that both TE and TM have regions where small changes in angle of incidence lead to large variations in coupling coefficients. This variation in coupling coefficients will manifest itself as a change in the mode shape on the far side of the trench, which will not match a propagating mode for the waveguide. The new power distribution will then radiate a portion of its power away and resolve back into a propagating mode. The radiated power will be seen as loss through the coupler. Since modes in waveguides do not propagate parallel to the direction of the waveguide, but at the angle defined by the propagation vector, the angle of the trench on the waveguide will not be the angle of incidence seen by the mode. It is thus desirable to design a waveguide whose fundamental mode has a propagation vector well away from the regions where small angles lead to large variations in coupling coefficients.

In the optical coupler presented in Section 4, the $\beta$ vector of the fundamental mode propagates at an angle of 19.2°. This makes the angle of incidence of the mode upon the trench values of either 25.8° or 64.2°. Both of these values are outside of the asymptotic region of operation for the coupler.

## 6. Conclusion

A compact, high-efficiency optical coupler based on FTIR was presented. Because of its compact footprint, the coupler lends itself to integration into existing photonic circuit fabrication techniques. Increasing photonic integration will reduce size and cost and increase production yields and performance. Optical signal processors based on such PICs will

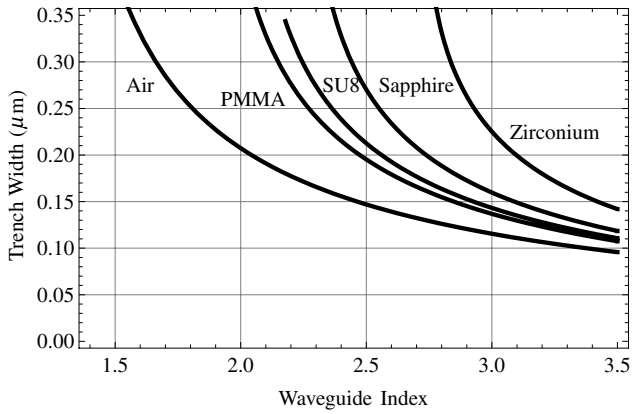


Fig. 10. Trench width required for 50% coupling of TE field as waveguide index varies for multiple trench index fills. Air, $n = 1$; PMMA, $n = 1.48$; SU-8, $n = 1.57$; sapphire, $n = 1.75$; $Zr0_2$, $n = 2.1$.

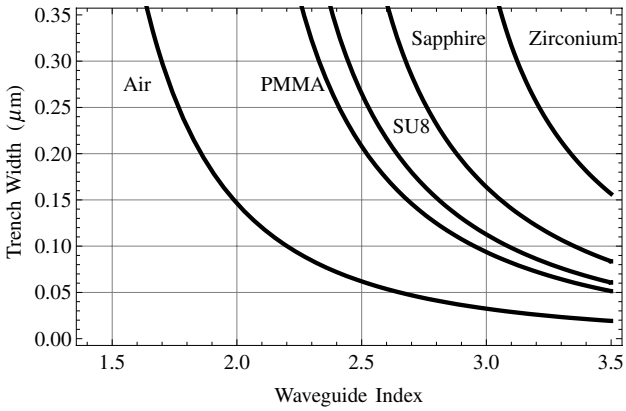


Fig. 11. Trench width required for 50% coupling of TM field as waveguide index varies for multiple trench index fills. Air, $n = 1$; PMMA, $n = 1.48$; SU-8, $n = 1.57$; sapphire, $n = 1.75$; $Zr0_2$, $n = 2.1$.

benefit from reduced response times and increased bandwidths.

From the parametric investigation of the coupler some interesting trends are seen. The first is the difference between TE and TM responses to parameter changes. Figures 1 and 8–12 show that while both TE and TM have regions of nonlinear behavior, the TE trend lines, in general, have a smaller slope. From this it is noted that TE polarized light is less sensitive to small changes in the design of the coupler. This makes TE a better choice for a coupler that is stable under a wide variety of operating conditions. TE's lack of sensitivity to coupler parameters is also important when considering fabrication tolerances. The manufacturing of large quantities of couplers with equivalent behavior requires less rigorous tolerances if TE polarization is used.

The higher sensitivity of TM light makes it an appealing choice for some applications. In particular, using the coupler as an integrated optical sensor is an area currently being investigated by the authors. It can be beneficial for sensors to operate in regimes

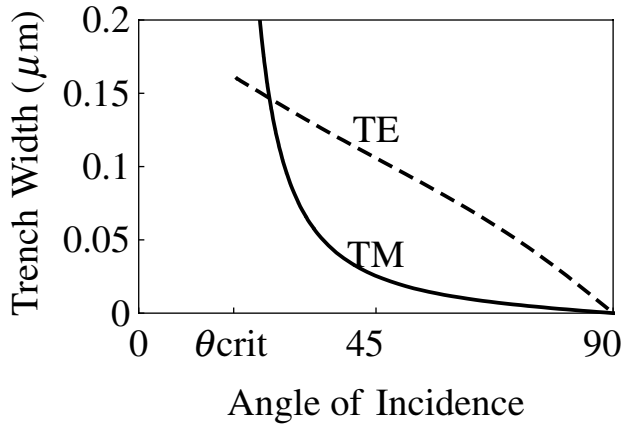


Fig. 12. Trench width required for 50% coupling as angle of incidence changes from 0°–90°. Waveguide index $n = 3.22$, trench index $n = 1$, $\theta_{crit} = 18.09°$. Dashed curve, TE; solid curve, TM.

where small changes of a parameter induce large changes in output.

As was pointed out in Section 5, it is also possible to design a coupler that is polarization independent. Through careful selection of waveguide, the trench index of refraction, and the angle of incidence, a coupler can be designed which has the same trench width for 3 dB coupling for both TE and TM polarization. For multimode systems in particular, this is very beneficial.

The authors acknowledge the support of the Defense Advanced Research Projects Agency (DARPA) through grant HR0011-08-1-005. In addition, the authors would like to thank Dr. Jerome Butler for the use of his millimeter wave research laboratory and his aid in performing the discussed experiments.

## References

1. W. K. Burns, R. P. Moeller, C. H. Bulmer, and H. Yajima, "Optical waveguide channels in Ti-diffused LiNbO3," Appl. Opt. **19**, 2890–2896 (1980).
2. M. Kuznetsov, "Radiation loss in dielectric waveguide Y-branch structures," J. Lightwave Technol. **3**, 674–677 (1985).
3. M. Maeda, T. Hirata, M. Surfiuro, M. Hihara, A. Yamaguchi, and H. Hosomatsu, "Photonic integrated circuit combining two GaAs distributed Bragg reflector laser diodes for generation of the beat signal," Jpn. J. Appl. Phys. **31**, L183 (1992).
4. T. D. Ni, D. Sturzebecher, A. Paolella, and B. Perlman, "Novel polymer optical couplers based on symmetry mode mixing," IEEE Photon. Technol. Lett. **7**, 1186–1188 (1995).
5. A. Hardy and W. Streifer, "Coupled mode theory of parallel waveguides," J. Lightwave Technol. **3**, 1135–1146 (1985).
6. J. P. Donnelly, H. Haus, and L. Molter, "Cross power and crosstalk in waveguide couplers," J. Lightwave Technol. **6**, 257–268 (1988).
7. M. Raburn, B. Liu, K. Rauscher, T. Okuno, N. Dagli, and J. E. Bowers, "3-D photonic circuit technology," IEEE J. Sel. Top. Quantum Electron. **8**, 935–942 (2002).
8. S. W. Ahn and S. Y. Shin, "Grating assisted codirectional coupler filter using electro-optic and passive polymer waveguides," IEEE J. Sel. Top. Quantum Electron. **7**, 819–825 (2001).
9. W. Huang, B. E. Little, and S. K. Chaudhuri, "A new approach to grating assisted couplers," J. Lightwave Technol. **9**, 721–727 (1991).
10. N. H. Sun, J. K. Butler, G. A. Evans, L. Pang, and P. Congdon, "Analysis of grating-assisted directional couplers using the Floquet–Bloch theory," J. Lightwave Technol. **15**, 2301–2315 (1997).
11. J. K. Butler, N. H. Sun, G. A. Evans, L. Pang, and P. Congdon, "Grating assisted coupling of light between semiconductor and glass waveguides," J. Lightwave Technol. **16**, 1038–1048 (1998).
12. S. Akiyama, M. A. Popovic, P. T. Rakich, K. Wada, J. Michel, H. A. Haus, E. P. Ippen, and L. C. Kimerling, "Air trench bends and splitters for dense optical integration in low index contrast," J. Lightwave Technol. **23**, 2271–2277 (2005).
13. S. Zhu, A. W. Yu, D. Hawley, and R. Roy, "Frustrated total internal reflection: a demonstration and review," Am. J. Phys. **54** , 601–607 (1986).
14. R. H. Renard, "Total reflection: a new evaluation of the Goos–Hänchen shift," J. Opt. Soc. Am. **54**, 1190–1197 (1964).
15. G. E. Musset, O. Boquilloin, and J. P. Forth, "High performance, diode pumped, *Q*-switched Er:Yb:glass laser with

FTIR shutter," in *Proceedings of the IEEE Conference on Lasers and Electro-Optics in Europe* (IEEE, 2000), p. 1.
16. I. N. Court and F. K. von Willisen, "Frustrated total internal reflection and applications of its principles to laser cavity design," Appl. Opt. **3**, 719–726 (1964).
17. D. Axelrod, "Cell-substrate illuminated by total internal reflection fluorescence," J. Cell Biol. **89**, 141–145 (1981).
18. D. J. Bossert, R. K. DeFreez, H. Ximen, R. A. Elliot, M. M. Hunt, G. A. Wilson, J. Orloff, G. A. Evans, N. W. Carlson, M. Lurie, J. M. Hammer, D. P. Bour, and S. L. Palfrey, "Grating-surface-emitting lasers in a ring configuration," Appl. Phys. Lett. **56**, 2068–2070 (1990).
19. E. Yablonovitch, T. J. Gmitter, and K. M. Yeung, "Photonic band structure: the face-centered-cubic case employing nonspherical atoms," Phys. Rev. Lett. **67**, 2295–2298 (1991).
20. R. A. Shelby, D. R. Smith, and S. Schultz, "Experimental verification of a negative index of refraction," Science **292**, 77–79 (2001).
21. K. L. Shlager and J. B. Schneider, "A selective survey of the finite-difference time-domain literature," IEEE Antennas Propagat. Mag. **37**, 39–56 (1995).
22. A. Taflove and S. C. Hagness, *Computational Electrodynamics, The Finite-Difference Time-Domain Method* (Artech House, 2005).
23. E. A. Navarro, T. M. Bordallo, and J. Navasquillo-Miralles, "FDTD characterization of evanescent modes—multimode analysis of waveguide discontinuities," IEEE Trans. Microwave Theory Technol. **48**, 606–610 (2000).
24. L. O'Faolain, M. V. Kotlyar, N. Tripathi, R. Wilson, and T. F. Krauss, "Fabrication of photonic crystals using a spin-coated hydrogen silsesquioxane hard mask," J. Vac. Sci. Technol. B **25**, 387–393 (2007).
25. H. Shin, D. Jeong, J. Lee, M. M. Sung, and J. Kim, "Formation of $TiO_2$ and $ZrO_2$ nanotubes using atomic layer deposition with ultraprecise control of the wall thickness," Adv. Mater. **16**, 1197–1200 (2004).